1 Shape Optimization of a Photo Gun

1.1 Current approach with a C^{∞} NURBS

- original geometry and electrode boundary in Figure 1
- inside of the electrode is discretized as well, to compute the volume constraint, see Figure 2

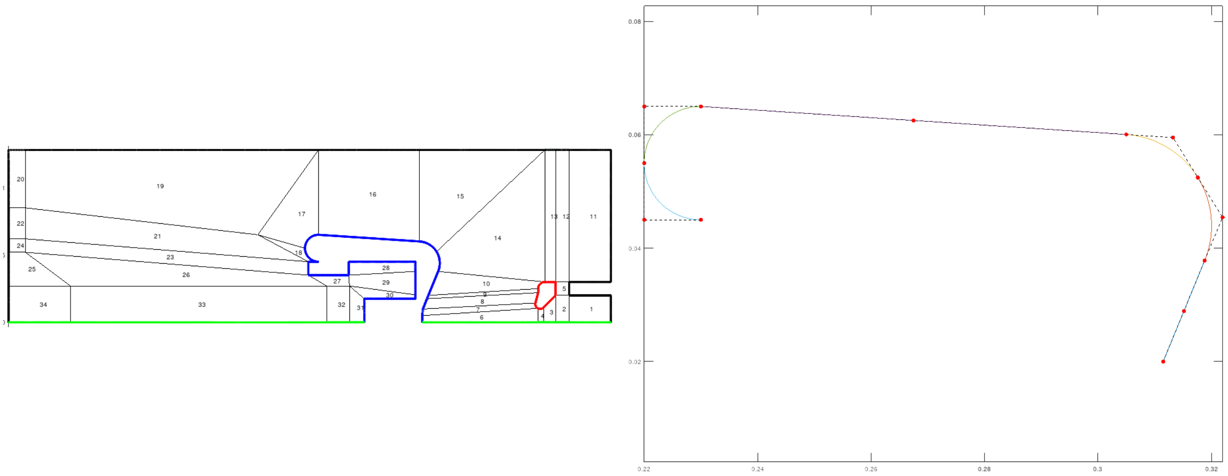

Figure 1: Original geometry and electrode boundary.

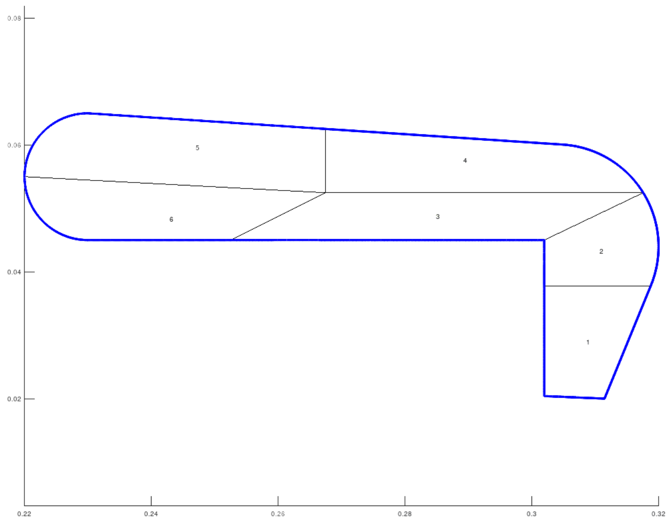

Figure 2: Discretization of the electrode.

- initial NURBS is formed by taking a subset of the control points of the original boundary, see Figure 3
- patch boundaries are chosen by finding the intersections of the original patch boundaries with the deformed NURBS (based on bisection method)
- bounds for the optimization are based on the patch boundaries (seemingly does not affect the results, since no control point is very close to any of the bounds), see Figure 4

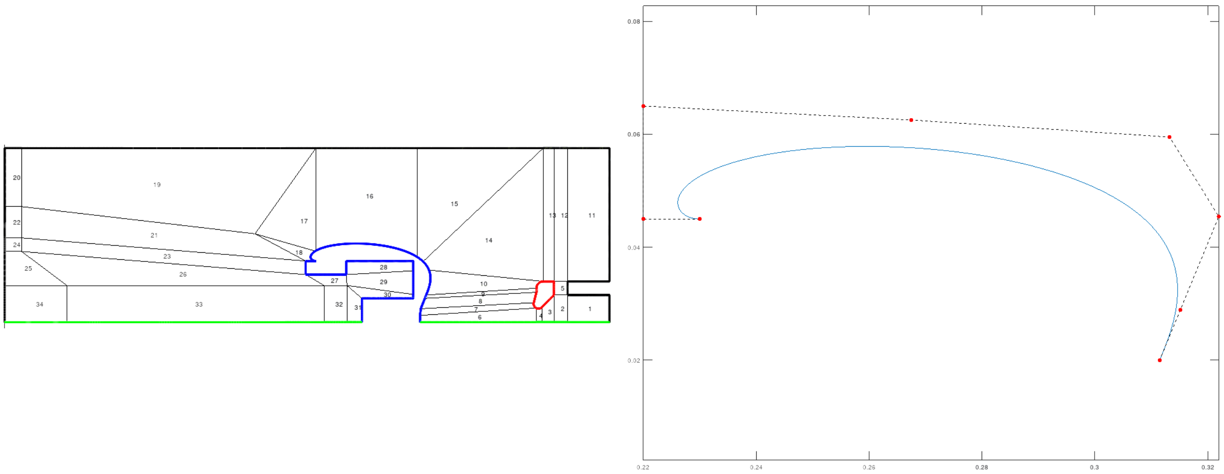

Figure 3: Initial geometry and NURBS.

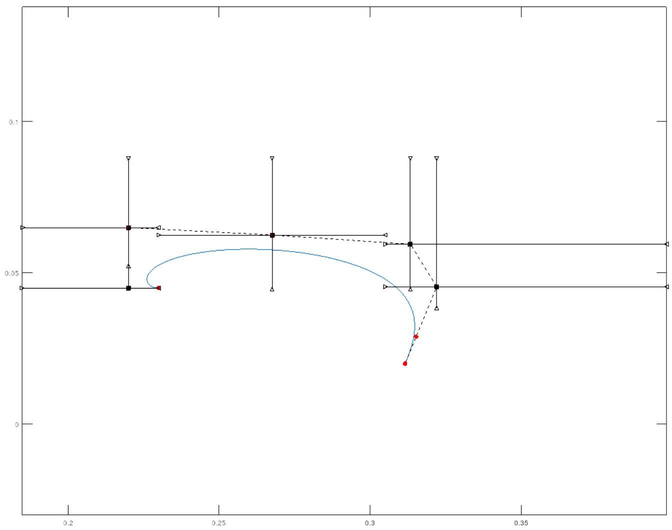

Figure 4: Bounds on the control points during the optimization.

- cost function looks at patches $14, \ldots, 18$
- cost function for the optimization is only based on the absolute maximum, i.e. $\max_{\mathbf{x}\in\Omega} \|\mathbf{E}(\mathbf{x})\|_2$
- optimized geometry and NURBS in Figure 5
- **results**:

	$(V_{\mathrm{el}} - 625)$ in cm^3	$\max_{\mathbf{x}\in\Omega} \|\mathbf{E}(\mathbf{x})\|_2$ in $\frac{\mathrm{MV}}{\mathrm{m}}$ (IGA)	$\max_{\mathbf{x}\in\Omega} \|\mathbf{E}(\mathbf{x})\|_2$ in $\frac{\mathrm{MV}}{\mathrm{m}}$ (CST)
original	5.541	12.745	13.116
initial	-310.945	11.968	
optimized	0.081	9.1	?

- corresponding electric field (IGA) for $p = 2$, $n_{\mathrm{sub}} = 128$, $V_{\mathrm{el}} = -300$ kV and $V_{\mathrm{ar}} = 1$ kV, see Figure 6
- corresponding electric field (CST) for second order tetrahedral elements, see Figure 7

Figure 5: Optimized geometry and NURBS.

Figure 6: Electric field of original and optimized geometry computed with GeoPDEs.

Figure 7: Electric field of original and optimized geometry computed with CST.

1.2 Tracking

- **general settings**: $Q = 100$ fC
- **spatial distribution**: see Figure 8 for distribution generated from measurement and for comparison with laser measurement
- see Figure 9 for spatial distribution from Gaussian ($\sigma = 400$ μm)
- **temporal distribution**: Gaussian with $\sigma = 5$ ps (is measurement data available?)

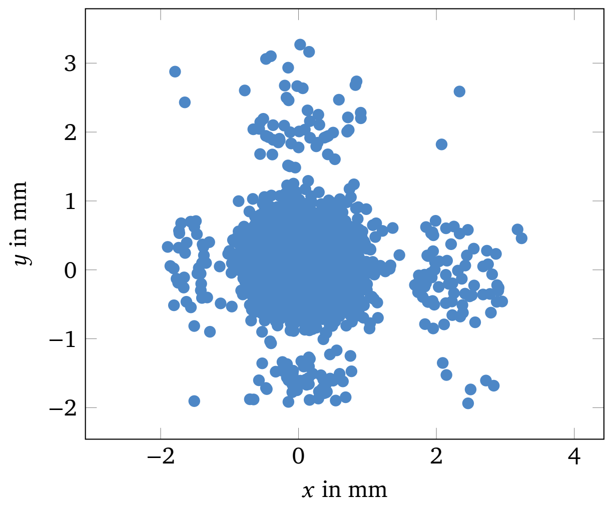

Figure 8: Spatial distribution generated from measurement (2^{11} particles) and laser measurement.

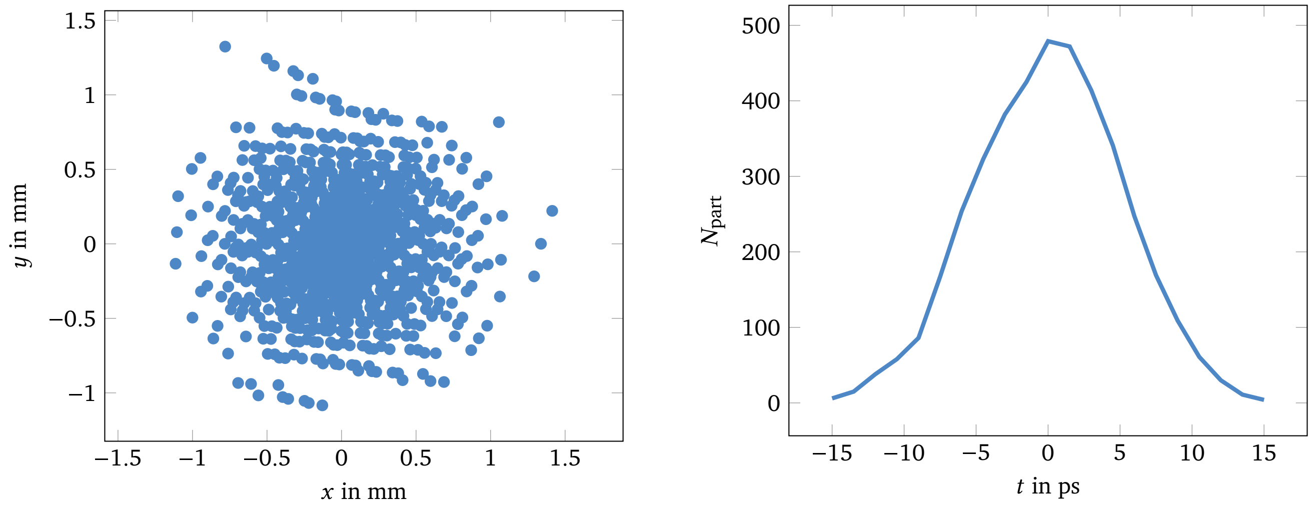

Figure 9: Spatial distribution from Gaussian ($\sigma = 400$ μm, 2^{10} particles) and temporal distribution (2^{11} particles).

- **convergence of time integrator**: relative error of normalized transverse emmitance ϵ w. r. t. finest time step is shown in Figure 10
- computed with $n_x = n_y = 8$ ($h_x = h_y = 1.875 \cdot 10^{-4}$) and $n_z = 256$ ($h_z = 4.258 \cdot 10^{-4}$)
- $H = 2^{-12}$ ns used later on

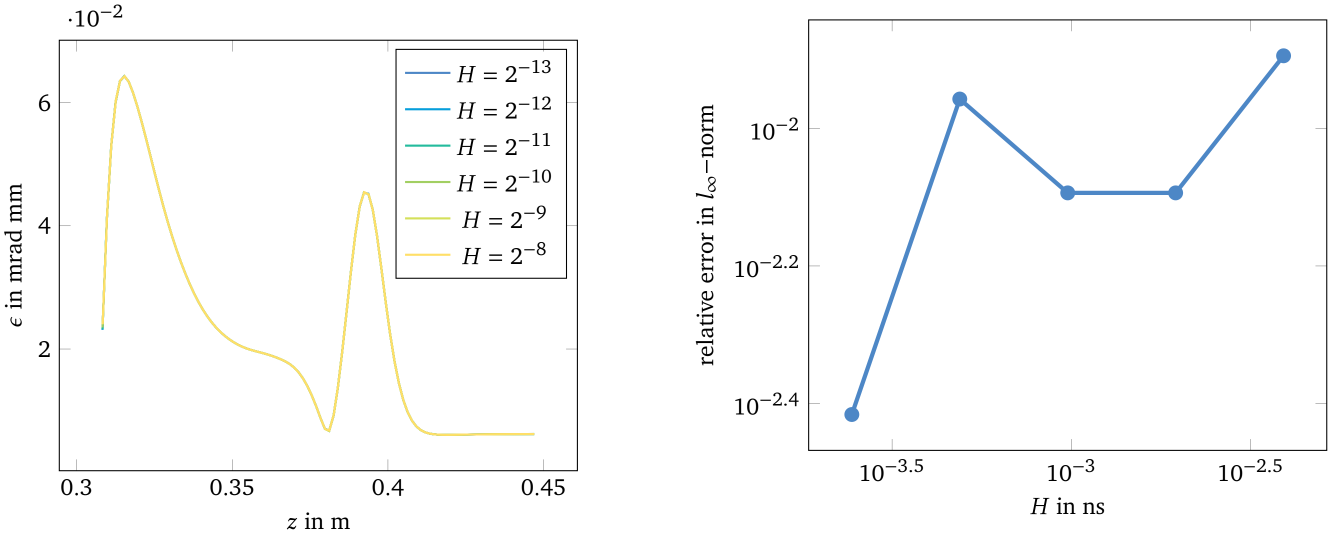

Figure 10: Normalized transverse emmitance and relative error in l_∞-norm.

- **convergence of field map**: look at convergence with number of grid points in transverse (n_x, n_y) and longitudinal (n_z) direction individually
- Figure 11 looks at convergence of n_x, n_y for $n_z = 64$ ($h_z = 1.703 \cdot 10^{-3}$)
- Figure 12 looks at convergence of n_z for $n_x = n_y = 8$ ($h_x = h_y = 1.875 \cdot 10^{-4}$)
- $n_x = n_y = 8$ ($h_x = h_y = 1.875 \cdot 10^{-4}$) and $n_z = 256$ ($h_z = 4.258 \cdot 10^{-4}$) used for convergence studies later on
- $n_x = n_y = 16$ ($h_x = h_y = 2.5 \cdot 10^{-4}$) and $n_z = 256$ ($h_z = 4.258 \cdot 10^{-4}$) used for simulation later on (distribution from measurement is larger then that from Gaussian by more then a factor 2, see Figure 8 and Figure 9)

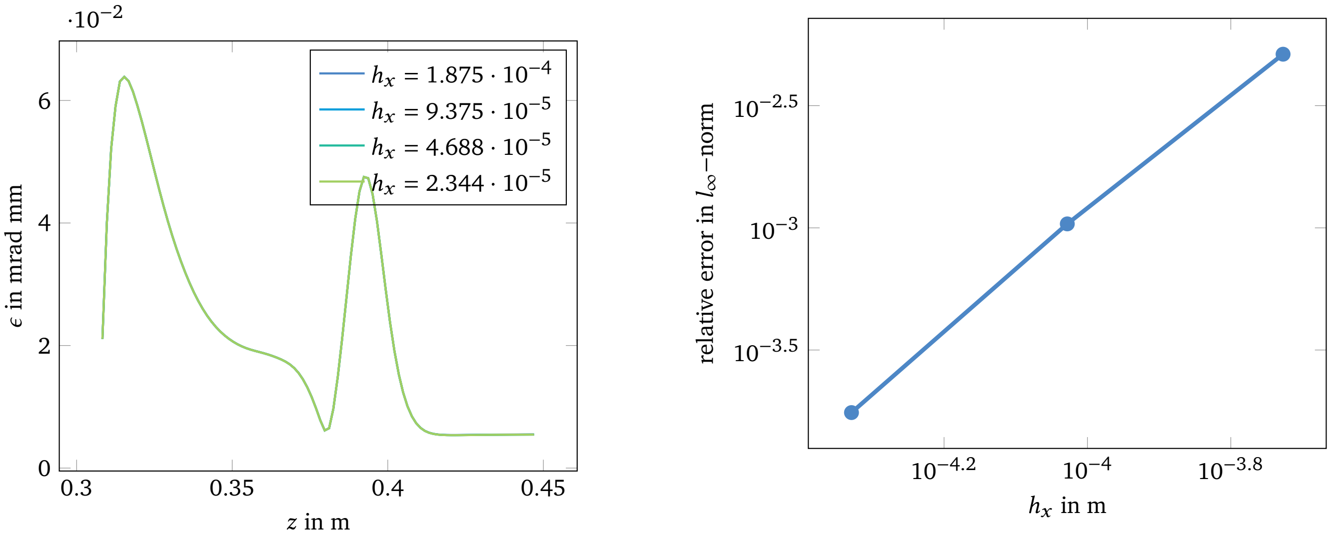

Figure 11: Normalized transverse emmitance and relative error in l_∞-norm for $n_z = 64$ ($h_z = 1.703 \cdot 10^{-3}$) and $n_x = n_y$ variable.

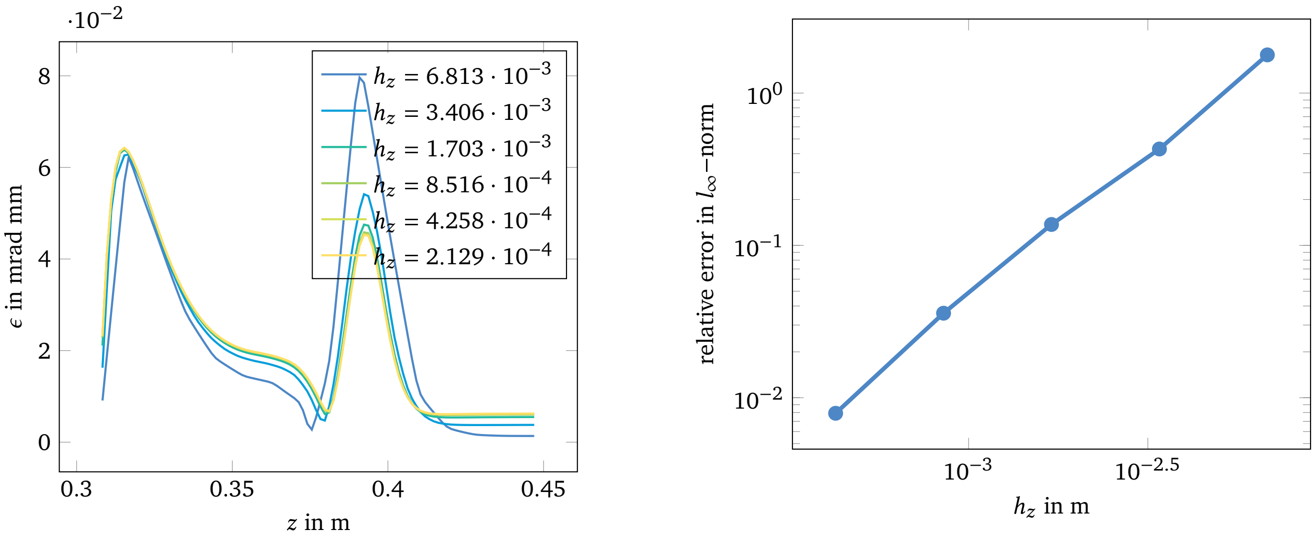

Figure 12: Normalized transverse emmitance and relative error in l_∞-norm for n_z variable and $n_x = n_y = 8$ ($h_x = h_y = 1.875 \cdot 10^{-4}$).

- **convergence of space charge**: look at convergence with number of grid cells in radial (n_r) and longitudinal (n_l) direction and number of particles (n_I) separately
- Figure ?? looks at convergence of n_r, n_l for $n_I = 2^{10}$
- $n_r = n_l = 64$ ($h_r = 2.344 \cdot 10^{-5}, h_l = 1.703 \cdot 10^{-3}$) used later on
- Figure ?? looks at convergence of n_I for $n_r = n_l = 64$ ($h_r = 2.344 \cdot 10^{-5}, h_l = 1.703 \cdot 10^{-3}$)
- $n_I = 2^{11}$ used for simulation later on

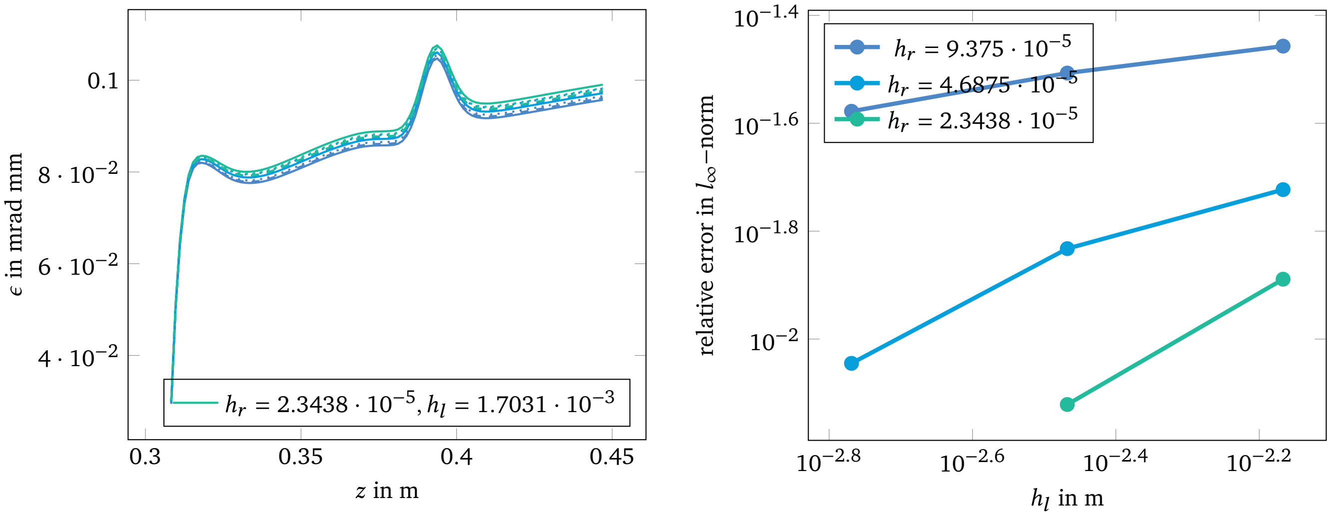

Figure 13: Normalized transverse emmitance and relative error in l_∞-norm for $n_I = 2^{10}$ and n_l, n_r variable.

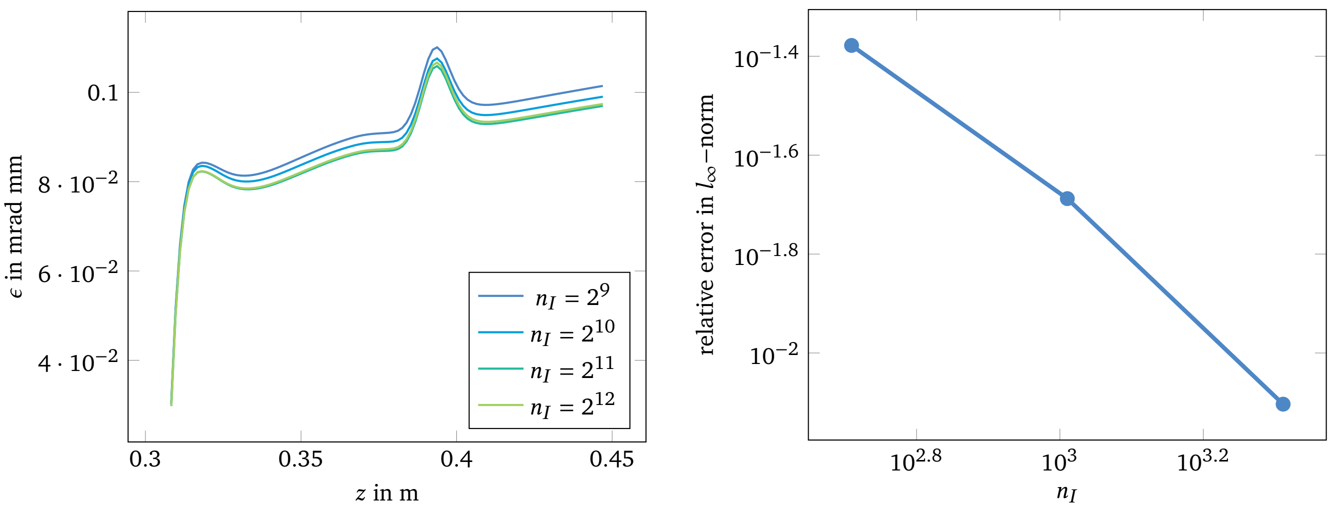

Figure 14: Normalized transverse emmitance and relative error in l_∞-norm for n_I variable and $n_r = n_l = 64$ ($h_r = 2.344 \cdot 10^{-5}, h_l = 1.703 \cdot 10^{-3}$).

- **tracking results**: simulation results for initial and optimized geometry
- continued tracking for 15 cm into the beam pipe
- initial normalized transverse emmitance for $H = 2^{-12}$, $n_x = n_y = 8$, $n_z = 256$, $n_r = n_l = 64$, $n_I = 2^{11}$ and refined ($H = 2^{-13}$, $n_x = n_y = 16$, $n_z = 512$, $n_r = n_l = 128$, $n_I = 2^{12}$) in Figure **??** (uses Gaussian distribution, $\tilde{\epsilon}$ signifies refined solution)
- optimized normalized transverse emmitance for $H = 2^{-12}$, $n_x = n_y = 16$, $n_z = 256$, $n_r = n_l = 64$, $n_I = 2^{11}$ also in Figure **??** (uses distribution from measurement)
- rms beam size of initial geometry in Figure **??**
- rms beam size of optimized geometry in Figure **??**
- **results**:

	relative error of ϵ in l_∞−norm	relative error of x_{rms} in l_∞−norm
x	$3.38 \cdot 10^{-3}$	$6.046 \cdot 10^{-3}$
y	$4.277 \cdot 10^{-3}$	$1.027 \cdot 10^{-2}$

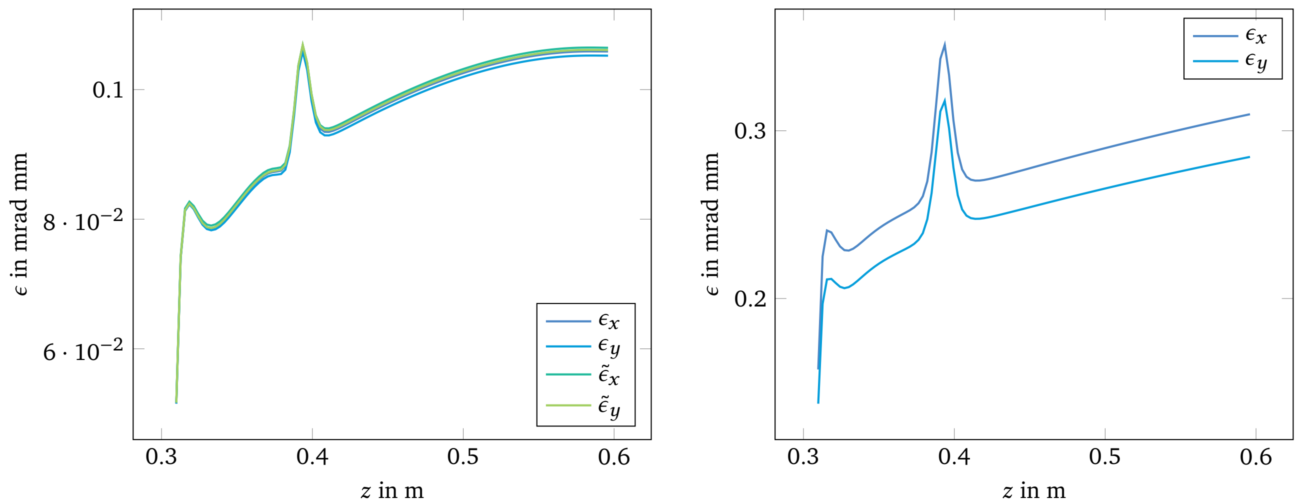

Figure 15: Normalized transverse emmitance of initial and optimized geometry.

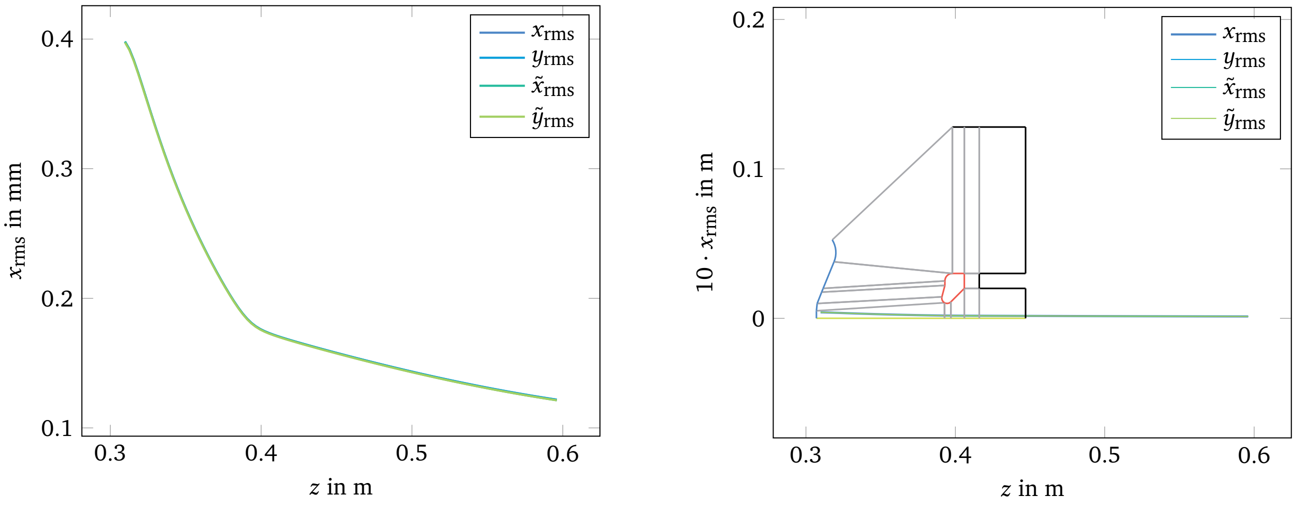

Figure 16: RMS beam size of initial geometry.

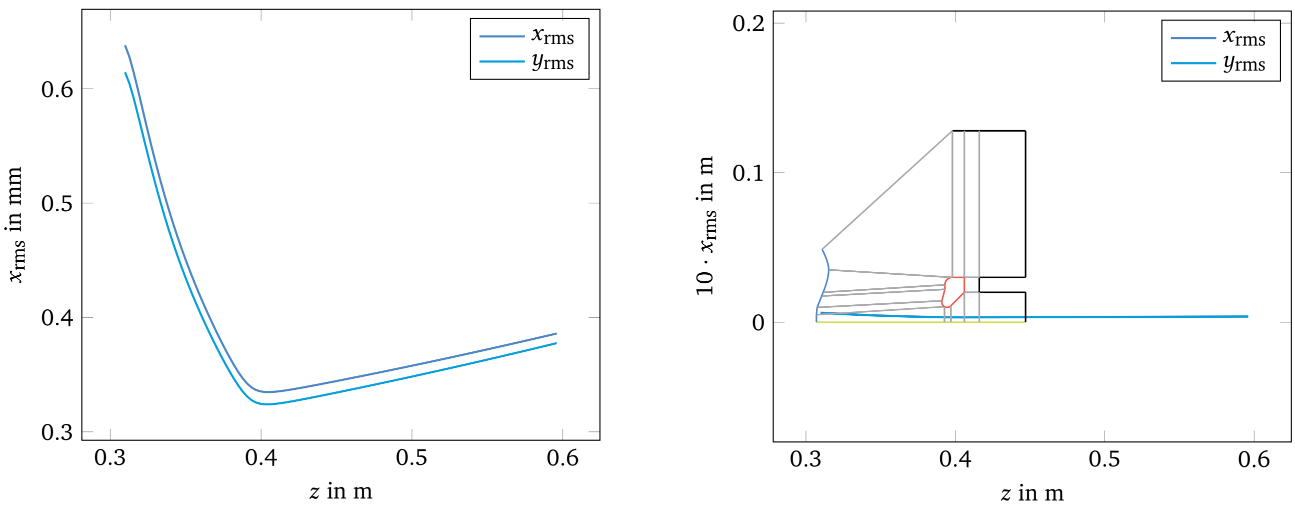

Figure 17: RMS beam size of optimized geometry.

References

[1] Markus Wagner. “Production and investigation of pulsed electron beams at the S-DALINAC”. PhD thesis. Technische Universität Darmstadt, 2013.